

An Optimal Operation of a Free-Standing Foucault Pendulum

Toshinori Michishita* and Teruo Takahashi

Graduate School of Human and Environmental Studies, Kyoto University, Kyoto 606-8501, Japan

This paper presents a new strategy which allows us to achieve a successful Foucault pendulum with a portable and free-standing device developed. A numerical calculation for the two-dimensional Hamilton's equations predicted that the pendulum realizes the ideal Foucault performance when the time-averaged action vanishes. Experimental results strongly confirmed the numerical prediction from measurement of the action as a function of the distance between the control magnets. The device has performed the Foucault pendulum with the sufficiently accurate and reliable rotation rates corresponding to the latitudes. Independency of latitude for the optimal condition to the device was verified by the measurement of the rotation rates of the pendulum at different latitudes. Limit cycle and locking phenomena for the pendulum rotation were observed depending on the distance between the magnets. A criterion for their occurrences was examined by using the Adler equation.

Keywords:

Foucault pendulum, Hamilton's equations, optimal condition, independency of latitude, limit cycle, locking phenomenon

1. Introduction

In 1851 Leon Foucault demonstrated the Earth's rotation with a 67m wire in length and a 28kg bob in weight at the Pantheon in Paris.¹⁾ Apropos of a Foucault pendulum, most people may recall up large-scale devices which are displayed in the halls of museums and the universities.²⁾ Most of their massive devices are provided exclusively for demonstration of the Earth's rotation and are scarcely utilized for studying dynamics in greater detail.

Moderate or small Foucault pendulums, on the other hand, have been developed not only for education but also for investigations on nonlinear dynamics such as phase-lock phenomenon and chaos.³⁻⁵⁾ Reductions both in length and in weight of a pendulum bring about undesirable effects in rotation of the plane of oscillation, resulting in *terrible* rotation far from "ideal" Foucault one. The most serious problem to overcome is restraint of undesirable rotation due to elliptical motion of the plane of oscillation.^{6,7)}

Recently several authors have developed moderate or small pendulums showing the ideal Foucault rotation, which are continuously operated with the electromagnetic drive.⁸⁻¹⁰⁾ In order to operate "ideal" Foucault performance, they eliminated the elliptical motion itself of the plane of oscillation with a Charron ring and restrained the increase of undesirable rotation rate due to the elliptical motion with a pair of permanent magnets forming the repulsive magnetic field. Instead of the damping method with the Charron ring, the eddy current brake was applied for damping of the elliptical motion by several authors.^{11,12)}

Hecht analyzed the motion of the free pendulum using the action-angle variable perturbation theory and compared the rotation rates measured by Crane with his analyzed ones.¹³⁾ In the analysis he supposed that the pendulum was free and azimuthally symmetric, and that the fast and slow actions, which corresponded to the angular momenta of the oscillation and the rotation, respectively, still remained constant. He indicated that the optimal setting for the distance between the

magnets was determined by locating the intersection of rotation rate curves for both clockwise and counterclockwise elliptical motion.

We developed a portable and free-standing Foucault pendulum accompanied by the eddy-current brake. Our primary interest was how to determine such an optimal condition to realize an "ideal" Foucault performance for this pendulum. Under the optimal condition we performed a steady-state operation for this device with the reliable and accurate Foucault rotation rate.

The next section describes analysis for realizing a successful Foucault pendulum. For the purpose we analyze the pendulum motion making use of the two-dimensional Hamilton's equations for an azimuthally asymmetric pendulum; two variables are the action and angle of the rotation. It is noted that in the analysis the rotation-associated action is treated as time-varying variable different from that in reference.¹³⁾ According to Hecht, we make use of the perturbation theory with the control permanent magnets in the terms of the action-angle variables. Besides the magnet effect, we now introduce asymmetric potential effect and damping effect perpendicular to the plane of oscillation due to the eddy current brake into the Hamilton's equations. Depending on the relevant parameters, the pendulum exhibited periodic or non-periodic motion. We show that the pendulum achieved the successful Foucault rotation when the time-averaged canonical action vanished. A brief observation as reported in the references^{10,13)} would not be capable of such determination.

The third section describes a setup of a portable and free-standing device and experimental results. A motion of the pendulum was observed with a webcam from the upper onto the pendulum bob. Measurements of barycentric coordinates of the bob enabled the detailed analysis of temporal behaviors of the angular momentum of the pendulum and the rotation angle of the plane of oscillation. Once the optimal condition is experimentally known, we are able to adjust the relevant control parameter on the pendulum to make "ideal" Foucault performance even at different latitudes. This might bring significant benefits in developing Foucault pendulum devices, for an example, for education.

Limit cycle and locking phenomena for the pendulum rotation were observed depending on the

distance between the control magnets. A criterion for their occurrences was examined by using the Adler's equation derived from the perturbed Hamilton's equations. The final section is devoted to conclusion.

2. Analysis for "Ideal" Foucault Pendulum Performance

Dynamics of the Foucault pendulum was analyzed by taking into account of the following effects; 1) the Coriolis force causing rotation of the plane of oscillation of the pendulum, 2) the elliptical motion due to the nonlinear effect, 3) the Crane-type repulsion force between the permanent magnets^{9,10)} for removing the undesirable rotation, and 4) the asymmetric effects of the system, which might be resulted from support at the upper end of wire suspending a bob, the error in the positioning of the driving coil, and the residual deviation of the axis of the copper annular disk for the eddy current brake.

We supposed that in the steady state the energy gained from the magnetic driving force was compensated by the energy lost due to the air friction and the eddy current brake in the major direction of the plane of oscillation over one period of rotation of the pendulum. Moreover the driving system of the push-pull voltage adopted for the device, in principle, brought about no significant effect to the rotation rate. We, however, retained the damping effect in the transversal component of motion due to the eddy current brake.

2.1 Theoretical model

To describe motion of a spherical pendulum shown in Fig. 1.(a), the center-of-mass of the pendulum is given by the following spherical coordinates (ℓ_0, θ, ϕ) ;

$$\left. \begin{aligned} x &= \ell_0 \sin \theta \cos \phi, \\ y &= \ell_0 \sin \theta \sin \phi, \\ z &= \ell_0(1 - \cos \theta) \end{aligned} \right\} \quad (1)$$

With the magnetic and asymmetric perturbed potentials, V_{Mag} and V_{Asym} , respectively, we have the Hamiltonian given by,

$$H = \frac{1}{2m\ell_0^2} \left(p_\theta^2 + \frac{p_\phi^2}{\sin^2 \theta} \right) + mg\ell_0(1 - \cos \theta)$$

J_θ and J_ϕ .

$$J_\theta = \frac{1}{2\pi} \oint d\theta p_\theta, \quad J_\phi = \frac{1}{2\pi} \oint d\phi p_\phi. \quad (9)$$

The further canonical transformation of $J_1 = J_\theta + |J_\phi|$ and $J_2 = J_\phi$ yields the zeroth-order Hamiltonian given by

$$H_0 = \omega_0 J_1 = E. \quad (10)$$

For a classical oscillation, we have $E = 1/2 \cdot m\omega_0^2 (a^2 + b^2)$, where a and b are the major and minor semi-radii of the ellipse, respectively.

The Hamilton's characteristic function S_0 is

$$\begin{aligned} S_0 &= \oint d\theta p_\theta + \oint d\phi p_\phi \\ &= \phi J_2 + m\omega_0 \ell_0^2 \int \frac{d\theta}{\theta} \\ &\quad \times \left[-\theta^2 + \frac{2J_1\theta^2}{m\omega_0 \ell_0^2} - \frac{J_2^2}{m^2\omega_0^2 \ell_0^4} \right]^{\frac{1}{2}}. \end{aligned} \quad (11)$$

The new angle variables of ψ_1 and ψ_2 related to J_1 and J_2 , respectively, are given by

$$\psi_1 = \frac{\partial S_0}{\partial J_1}, \quad \psi_2 = \frac{\partial S_0}{\partial J_2}. \quad (12)$$

Performing the complicated but well-known calculation,^{13,14)} we can write down the perturbed Hamiltonian in the terms of the fast and slow action-angle variables of $(\psi_1, \psi_2, J_1, J_2)$, which is given by

$$\begin{aligned} H_1 &= \frac{J_2}{6m\ell_0^2} - \Omega_F J_2 - \frac{J_1^2}{24m\omega_0^2 \ell_0^2} \\ &\quad \times \left[1 - \left(1 - \frac{J_2^2}{J_1^2} \right)^{1/2} \cos 2\psi_1 \right]^2 \\ &\quad + V_{\text{Mag}}(\psi_1, J_1, J_2) + V_{\text{Asym}}(\psi_1, \psi_2, J_1, J_2) \end{aligned} \quad (13)$$

where V_{Mag} corresponds to eq.(8) with the components of

$$V_{1,\text{Mag}} = \frac{q_M^2}{4\pi\mu_0}$$

$$\times \frac{1}{\left\{ d^2 + \frac{\ell(d+\ell)J_1}{m\omega_0^2 \ell_0^2} \left[1 - \left(1 - \frac{J_2^2}{J_1^2} \right)^{1/2} \cos 2\psi_1 \right] \right\}^{1/2}}. \quad (14)$$

The asymmetric potential is rewritten in the terms of the action- angle variables (see Appendix) as follows;

$$\begin{aligned} V_{\text{Asym}} &= \delta_0 \Omega_F J_1 \cos 2\psi_2 \left(\cos 2\psi_1 - \left[1 - \frac{J_2^2}{J_1^2} \right]^{1/2} \right) \\ &\quad + \sigma \delta_0 \Omega_F J_1 \sin 2\psi_2 \left| \frac{J_2}{J_1} \right| \sin 2\psi_1. \end{aligned} \quad (15)$$

Now we have the Hamilton's equation of motion given by

$$\dot{\psi}_1 = \frac{\partial H_0}{\partial J_1} = \omega_0, \quad \dot{J}_1 = -\frac{\partial H_0}{\partial \psi_1} = 0, \quad (16)$$

$$\dot{\psi}_2 = \frac{\partial H_1}{\partial J_2}, \quad \dot{J}_2 = -\frac{\partial H_1}{\partial \psi_2}. \quad (17)$$

From the zeroth-order equation we directly obtain the angle variable $\psi_1 = \omega_0 t$ and the action variable $J_1 = \text{const}$. It is sufficient that the slow variables are calculated after time-averaging the perturbed Hamiltonian over the fast frequency period. Namely, the equations to be solved are given by

$$\dot{\psi}_2 = \frac{\partial \langle H_1 \rangle}{\partial J_2}, \quad \dot{J}_2 = -\frac{\partial \langle H_1 \rangle}{\partial \psi_2}. \quad (18)$$

where the bracket $\langle \dots \rangle = \int_0^{2\pi} d\psi_1 \dots$. Consequently we obtain the perturbed Hamilton's equations to be solved as follows:

$$\begin{aligned} \dot{\psi}_2 &= -\Omega_F + \frac{3J_2}{8m\ell_0^2} \left[1 - f_{\text{mag}}(d, \ell) \right] \\ &\quad + \delta_0 \Omega_F \cos 2\psi_2 \frac{J_2}{J_1} \left(1 - \frac{J_2^2}{J_1^2} \right)^{-1/2} \end{aligned} \quad (19)$$

$$\dot{J}_2 = -\lambda J_2 - 2\delta_0 \Omega_F \sin 2\psi_2 J_1 \left(1 - \frac{J_2^2}{J_1^2} \right)^{1/2} \quad (20)$$

Here $f_{\text{mag}}(d, \ell)$ represents the magnet effect, which is described in the form of infinite series¹³⁾

and is given by

$$f_{\text{mag}}(d, \ell) = f(d, \ell) + f(d+h; \ell-h) - f(d+h; \ell) - f(d+2h; \ell-h), \quad (21)$$

where

$$f(d, \ell) = \frac{4}{3} \frac{q_M^2}{4\pi\mu_0\bar{d}} \frac{m\ell_0^2}{J_1^2} \sum_{n \geq 1, \text{odd}} \binom{3}{2}_n \frac{(n+1)\Delta^{n+1}}{2^{n+1} \left[\left(\frac{n+1}{2} \right)! \right]^2}, \quad (22)$$

with

$$\bar{d}^2 = d^2 + \frac{\ell(\ell+d)J_1}{m\omega_0\ell_0^2}, \quad \Delta = \frac{\ell(d+\ell)}{\bar{d}^2} \frac{J_1}{m\omega_0\ell_0^2}. \quad (23)$$

It is noted that the dissipation term in eq.(20) is empirically introduced for the action variable J_2 , of which the damping coefficient will be given in the next section. The asymmetric effect is described in the above equations of (19) and (20). Therefore the slow action variable J_2 is no longer treated as constant, in contrast to the case in the reference.¹³⁾ As shown in the next subsection, it is difficult to predict the optimal setting for the distance between the magnets by locating the intersection of rotation rate curves for both the clockwise and counterclockwise elliptical motions. Because the rotation rate curves for both clockwise and counterclockwise elliptical motions *did not* intersect each other. An alternative method will be presented for "ideal" Foucault pendulum performance.

2.2 Numerically calculated results

We focus on the dependence of slow variables, namely, the angle ψ_2 and the action J_2 on the distance between the control magnets. Hereafter the distance " d_{opt} " denotes one at which the magnetic effect nullifies the undesirable rotation due to the elliptical motion. In the references,^{10,13)} the optimal setting for d_{opt} was determined by locating the intersection of rotation rate curves for both clockwise and counterclockwise elliptical motion from a brief observation every five minutes. Our method for locating d_{opt} was quite different from that in the references, as will be seen in the present subsection no such intersection was observed.

Mathematica programs led easily to the numerical solutions for ψ_2 and J_2 with the initial con-

ditions, without losing generality, of $\psi_2(0) = 0$ and $J_2(0) = 0$. We adopted empirically the other parameters as follows: $q_M = 2.0 \cdot 10^{-5} \text{Wb}$, $\ell_0 = 943 \text{ mm}$, $h = 40 \text{ mm}$, $a = 36.5 \text{ mm}$, $b = 0.5 \text{ mm}$, $\delta_0 = 0.2 \sim 0.5$, and $\lambda = 2 \text{ h}^{-1}$. Here the intensity of the magnetic pole, q_M , was obtained by detecting a spatial intensity profile with a gauss meter. The latitude was adopted to $35^\circ 01' N$ at an experimental laboratory of the Kyoto University.

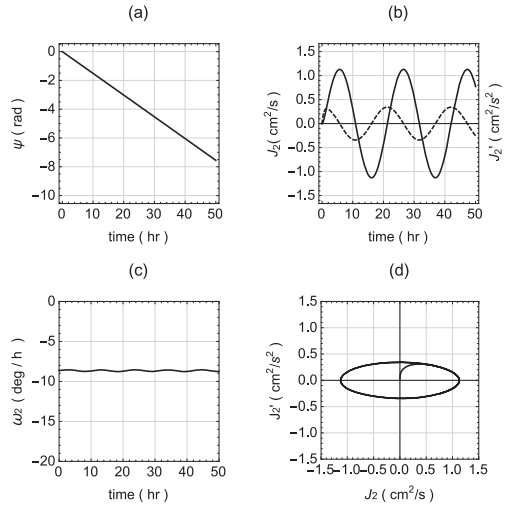


Fig. 3. Analytical Results for the approximately optimal case of $\langle J_2 \rangle \simeq 0$ for the parameters of $d = 59 \text{ mm}$, $\lambda = 2 \text{ h}^{-1}$ and $\delta_0 = 0.4$; (a) temporal behavior of rotation angle of the plane of oscillation, (b) temporal behaviors of slow action variable J_2 per unit mass (solid curve) and its derivative \dot{J}_2 (broken curve), (c) rotation rate of the plane of oscillation, (d) trajectory in phase space (J_2, \dot{J}_2). It is noted in (c) that a harmonic oscillation with small amplitude emerges in rotation rate due to the asymmetric effect.

Figure 3 shows the approximately optimal case with the distance of $d = 59 \text{ mm} (\simeq d_{\text{opt}})$. As shown in Fig.3(a), the rotation angle ψ_2 linearly decreased with a time. Its gradient gave the average rotation rate, $\langle \omega_2 \rangle$, which was -8.63 deg/h . The rotation rate showed an excellent agreement with the theoretical values, $\omega_{2,\text{opt}} \equiv -\Omega_F = -\Omega_e \cdot \sin \alpha = -8.63 \text{ deg/h}$ with $\alpha = 35^\circ 01' N$. As shown in Fig.3(b), the action variable J_2 per unit mass had a sinusoidal waveform with a second harmonic oscillation to the rotation rate. It is noted that in the case of $d \simeq d_{\text{opt}}$ the rotation rate exhibited a fourth harmonic oscillation with a small

amplitude as seen in Fig.3(c). This resulted from the asymmetric effect described in the third term of r.h.s. in the eq.(19). Furthermore we can see a stable limit-cycle motion as shown in Fig. 3(d).

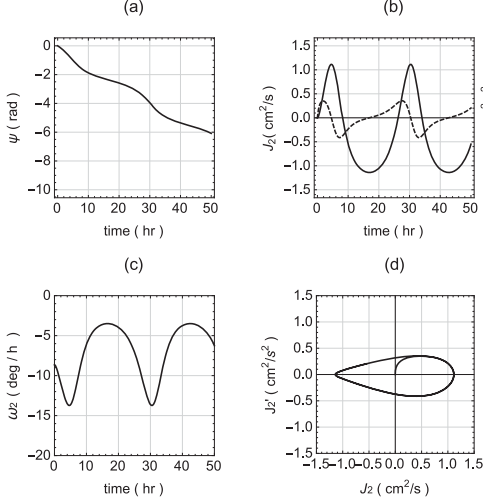


Fig. 4. Analytical Results for the case of $\langle J_2 \rangle < 0$ per unit mass for the parameters of $d = 54$ mm, $\lambda = 2\text{h}^{-1}$ and $\delta_0 = 0.4$; (a) temporal behavior of rotation angle of the plane of oscillation, (b) temporal behaviors of slow action variable J_2 per unit mass and its derivative \dot{J}_2 , (c) rotation rate of the plane of oscillation, (d) trajectory in phase space (J_2, \dot{J}_2).

When the distance, d , was set out of, but not very far from the optimal one, d_{opt} , the rotation angle exhibited a temporal behavior with a wavy line as shown in Fig.4(a). Its rotation rate was $\langle \omega_2 \rangle = -7.95$ deg/h.

For the case of insufficiently nullifying the undesirable rotation due to the elliptical motion, the action J_2 and the rotation rate ω_2 varied largely in time as seen in Figs.4(b) and 4(c). In the case the rotation rate ω_2 varied out of phase with the action J_2 . For the other case of $d > d_{\text{opt}}$, ω_2 varied in phase with J_2 . In both the regions, the average rotation rates, $\langle \omega_2 \rangle$, became smaller in magnitude than that at $d = d_{\text{opt}}$, because averaging $J_2 \times (1 - f_{\text{mag}})$ in the second term of r.h.s. in eq.(19) over the rotation period always reduced the rotation rate. This was in contrast with the result in the other analysis.¹³⁾

Such numerical results of the temporal behaviors of the pendulum could be straightforwardly

predicted from the following analysis. Suppose that the solution for Eq.(20) is of form of $J_2^{\text{st}} = A \sin 2\psi_2 + B \cos 2\psi_2$ in a steady state. Substituting the equation into Eq.(20) and solving for the coefficients of A and B, the action was given by

$$J_2^{\text{st}} \approx A \sin 2 \left[\psi_2 + \frac{\Omega_F}{\lambda} \right], \quad A = -\frac{2\delta_0 \Omega_F J_1}{\lambda}. \quad (24)$$

where we adopted an approximation of $\lambda \gg \Omega_F$. In the analysis we made use of $\dot{\psi}_2 = \omega_2 \approx -\Omega_F$ at $d \simeq d_{\text{opt}}$. Neglecting contribution from the third term of r.h.s. in eq.(19) and substituting eq.(24) into J_2 in the second term of r.h.s. in eq.(19), the equation was rewritten as the Adler's equation¹⁵⁾, namely,

$$\frac{d\psi_2^*}{\Omega_F + \omega_b \sin 2\psi_2^*} = -dt, \quad (25)$$

where $\psi_2^* = \psi_2 + \Omega_F/\lambda$ and $\omega_b = 6\delta_0 \Omega_F J_1 \cdot (1 - f_{\text{mag}})/(8m\ell_0^2 \lambda)$. Carrying out the integration, we obtained the angle ψ_2^* as a function of time as follows:

$$\psi_2^* = -\tan^{-1} \left\{ |\beta| + \sqrt{1 - \beta^2} \tan \left[\Omega_F \sqrt{1 - \beta^2} t \right] \right\}. \quad (26)$$

where $\beta = \omega_b/\Omega_F$. From the equation, the rotation rate was determined from the time derivatives of the above ψ_2^* and is given by

$$\begin{aligned} \dot{\psi}_2 &= \omega_2 \\ &= -\frac{\Omega_F \left[(1 - \beta^2) \sec^2 \left[\Omega_F \sqrt{1 - \beta^2} t \right] \right]}{1 + \left[|\beta| + \sqrt{1 - \beta^2} \tan \left(\Omega_F \sqrt{1 - \beta^2} t \right) \right]^2}. \end{aligned} \quad (27)$$

For the case of exactly $d = d_{\text{opt}}$, the rotation rate was $\omega_2 = -\Omega_F$, and the rotation angle was $\psi_2 = -\Omega_F t$ with the initial condition of $\psi_2(0) = 0$ because of $\beta = 0$. It is noted that no oscillation in ω_2 was expected just at $d = d_{\text{opt}}$ because of neglecting the asymmetric effect in the analysis; the asymmetric effect influenced the rotation rate through the action J_2 . But practically the numerical result showed that the rotation rate had a small amplitude with a higher harmonic oscillation with a frequency of $4\Omega_F$ for the case of $d \simeq d_{\text{opt}}$ as

shown in Fig.3(c). This resulted from the asymmetric effect, which was neglected in the above analysis. The action J_2 , on the other hand, had a frequency of $2\Omega_F$. It implies that the action J_2 , which corresponded to the slow rotation rate, rotated twice while the pendulum rotated around the z -axis once.

Finally we turn to how to find out the optimal distance, d_{opt} . First we calculated the average rotation rate, $\langle\omega_2\rangle$, as a function of the distance. Figure 5 shows those for several values of the asymmetric coefficient δ_0 . It was practically difficult to clearly distinguish d_{opt} from other distances, where the pendulum performed the ideal Foucault rotation with the rate of $-\Omega_F$. The figure also shows the distance dependence of the action $\langle J_2 \rangle$. It exactly vanished at d_{opt} for all of the asymmetric coefficients, quite unlike $\langle\omega_2\rangle$. Consequently d_{opt} was the distance where $\langle J_2 \rangle = 0$. This method imposed consuming time for the measurement; it took at least 41 hours to measure $\langle J_2 \rangle$. Finding out such the distance as $\langle J_2 \rangle = 0$ required more than one week. It is emphasized that the optimum condition was not the result of artificially producing the ideal Foucault rotation rate, but the result of merely eliminating the undesirable rotation due to the elliptical motion. This would be experimentally verified through the measurement. Measurements at different latitudes with the same optimal condition, which is given in the next section.

It is noted that the locking phenomena could be observed when an inequality of $|\omega_b| \leq \Omega_F$ was satisfied. Such the locking phenomena will be examined in the following experimental results.

3. Experiments with a Foucault Pendulum

We focus on an optimal condition to realize the "ideal" Foucault rotation with the developed device, which was portable and free-standing for easy fabrication and removal. The device was utilized for performing Foucault rotation experiment at different latitudes to validate the above-mentioned prediction, as well as educational application.

3.1 Setup

Figure 6 shows a photograph of the pendulum whole. The cumulative height of the unit was 1.5 m. We adopted the similar system developed by

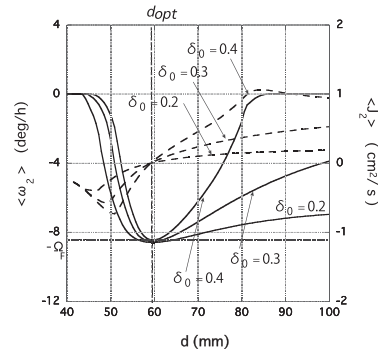


Fig. 5. Average rotation rate $\langle\omega_2\rangle$ for several values of the asymmetric coefficient δ_0 ($= \delta \cdot (\Omega_F/\omega_0)$) as a function of the distance, d , between the permanent magnets. With increasing in magnitude of the asymmetric parameter, δ_0 , the locking domain corresponding to $\dot{\psi}_2 = 0$ becomes wider. The solid and broken lines correspond to the cases of rotation frequencies and canonical angular momenta, respectively.

Crane,¹⁰⁾ namely, in which a permanent magnet was embedded at the bottom of the bob. His device was fixed on the wall, but our portable device was free-standing. For stability against various mechanical noises such as sound generated by air-conditioners, several lead blocks were put at the bottom of the device as an anchor.



Fig. 6. Photograph of the portable and free-standing pendulum device

The rectangular framework of the pendulum was fabricated from 30mm×30mm×1,500mm aluminum frames of which each has a raceway groove on each face for fixing. They were firmly fastened with lateral frames at the top, the medium, and the bottom.

The ceiling board provided a rectangular framework for supporting a wire, a LED lamp and a webcam. The board held the pendulum support, which was constituted of two triangular prisms and an annular disk as shown in Fig. 7. Both the prisms and the disk were made of carburized steel. Each prism was of 35 mm length and of a triangular section of one side of 10 mm. The disk was of 10 mm inner and 35 mm outer diameters, and 10 mm thick. The supporting point was set at the center of the air core of the annular disk. The moments of inertia around two axes of X and Y were slightly different in magnitude. This might lead to an asymmetric effect.

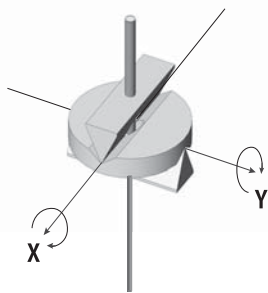


Fig. 7. The support for the pendulum bob made of two triangular prisms and an annular disk. The supporting point was set at the center of the annular disk. The lower prism was mounted on the ceiling board of the framework. Two axes of X and Y through the supporting point are shown.

The whole fabrication was covered with a blackout curtain to prevent air flow as well as to block obstructive lights radiated from the periphery for successful photographing. A LED lamp illuminated the interior of the framework for taking images of a pendulum bob with a webcam.

A piano wire of 0.8 mm diameter was used to suspend the bob and installed at the support. The distance from the supporting point to the center of the bob was 943 mm. The bob was a brass column of 60 mm in diameter, 100 mm in length and 2.4

kg in weight. A permanent magnet was embedded into the bottom. It was a cylindrical neodymium magnet of 5 mm diameter and 40 mm length, and its flux density was 0.49 T at the surface.

Figure 8 shows a diagram of the drive and measurement system. A board was installed at 20 cm above the bottom of the framework. An acrylic stem was mounted on the board for supporting drive and searching coils with air cores, and an annular copper disk (60 mm^{i.d.}×140 mm^{o.d.}×10 mm^t) for eddy current brake.

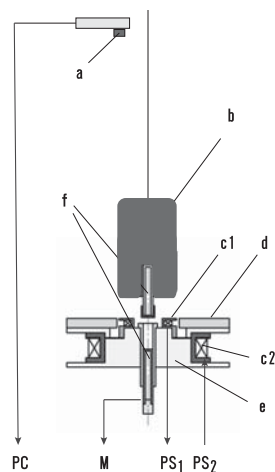


Fig. 8. Diagram of drive and measurement system; a: a webcam, b: a bob, c1: a searching coil, c2: a drive coil, d: a acrylic stem, f: neodymium magnets, PS1 and PS2: a power supply for searching and drive coils, respectively, M: an automatic drive system for moving the lower magnet, PC: a personal computer for measurement and analysis

The magnet embedded at the bottom of the bob was accelerated by an electromagnetic coil with push-pull type voltage, which was triggered by a signal detected with the small searching coil. The electromagnetic coil was 900 turns, which was made of 0.5 mm-diameter enameled wire, and its resistance was 106 Ω . The applied voltage required to drive the bob was typically 1 V, resulting in the excited current of the order of 10 mA. The electromagnetic-field detection coil was 2,300 turns, which was constituted by winding the 0.128 mm (1/200") diameter wire on a small acrylic bobbin. Its resistance was approximately 410 Ω . Both the coils were installed in a stem.

The annular copper disk was mounted above the

coils on the stem. The disk served to keep the amplitude of oscillation constant and to control the elliptical motion by damping the transversal component of motion of the pendulum. Replacing the mechanical method for the damping of motion of the pendulum with the electromagnetic one was indispensable for a long term operation. The damping coefficient in the longitudinal direction (the direction of the major axis of the ellipse), γ , could be obtained by turning off the driving power source and by observing damping of the major radius; typically $\gamma \approx 0.27 \text{ h}^{-1}$. The damping strength for the copper disk could be expressed using the quality factor Q , which was given by $Q = \omega_0 / (2\gamma)$ ($= (\text{oscillation energy}) / (\text{loss of oscillation energy per cycle})$). The damping effect by the eddy current depended on the space between the lower magnet and the copper disk. It was observed that the effect hardly changed in the case of the space less than 2.5 mm. In the present experiment, we set the space to 1 mm. Then we obtained approximately $Q \approx 5.5 \times 10^3$ in the region less than the inner radius of the disk, and $Q \approx 2.5 \times 10^3$ in the upper part of the disk: the energy loss of the pendulum was estimated as $E_{\text{loss}} \approx 9.4 \times 10^{-7} \text{ J/cycle}$ in the region without the disk, and $E_{\text{loss}} \approx 2.1 \times 10^{-6} \text{ J/cycle}$ in the upper part of the disk. Thus the damping was very effective for the action in the upper part of the disk.

When the lower magnet reached the maximum amplitude in the longitudinal direction, the brake due to the induced eddy current effectively acted on the transversal component of motion. The damping coefficient, λ , due to the induced eddy current was approximately 2 h^{-1} , which was measured at the time when an earthquake happened to cause the large displacement in the transversal direction.

The whole stem attached with the coils and the disk was mounted on a XY stage. Use of the instrument allows alignment to be accurately set the center axis of the coils and the pendulum bob. Using visual inspection combining with a digital camera capable of performing magnified images, we have an error of a fraction of 0.01 mm.

The lower magnet was set in the bottom of the acrylic stem for controlling the rotation. The magnet attached to an electric drive was automatically positioned by using a micro controller and a stepper motor. The automatic drive system changed

the distance between the magnets at every 2 mm, after measuring the barycentric coordinates of the bob for more than one period of the rotation. Its movable range was typically 30 mm from 40 mm to 70 mm. The system provided with an automatic operation function was very helpful to perform operations and updating from a remote location through a network.

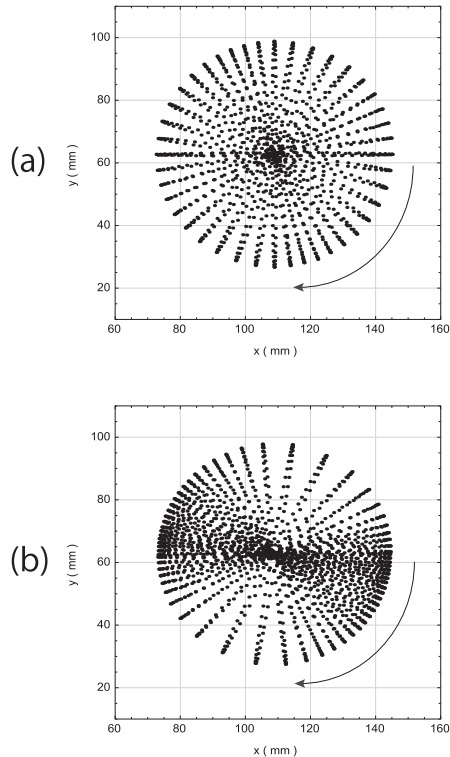


Fig. 9. Top views of hour-to-hour trajectories of the center-of-mass of the pendulum bob with a webcam; the two cases of (a) and (b) correspond to those of $d \approx d_{\text{opt}}$ and $d < d_{\text{opt}}$, respectively. The filled circles represent measured positions of the center of the bob. The trajectory at each measurement time formed a sufficiently thin ellipse. Each plane of oscillation rotated clockwise.

An object tracking method with a webcam was used for measurement of the barycenter of the bob. The camera had a frame rate of 15 ~ 30 fps and an image size of 640×480 pixels per frame. A spatial resolution was 0.347 mm/pixel, which assured a sufficient position analysis for motion of the bob. Each image to motion of the bob was photographed with 60 frames every five minutes. An

analysis of the image was capable to determine the barycenter coordinates of the bob. A PC program calculated the coordinates of the top area of the bob on the basis of the produced binarized image detected by the webcam, and saved the data on the PC while performing measurements. The PC program was made with the C++ language using the OpenCV package.¹⁶⁾ The program in Mathematica also allowed us to visualize the motion of the pendulum from the data on the PC.

3.2 Experimental results and discussions

We continuously performed the steady state operation and measured the center of the pendulum bob every 5 minutes with the webcam. In the case of much longer operations, it continued even more than one year.

Figure 9 shows top views of hour-to-hour trajectories of the barycentric coordinates during the half period of the pendulum rotation, which was approximately 21 hours in the present experiment. Figures 9(a) and 9(b) corresponded to the cases of $d \simeq d_{\text{opt}}$ and $d < d_{\text{opt}}$, respectively. In the figures, each trajectory of ellipse was drawn by overlaying 60 frames of the moving image; the shooting period was approximately 2 seconds. In Fig.9(a) we recognized that the plane of oscillation of the pendulum rotated with an equal advanced angle every hour. On the other hand, it took different advanced angles during the equal elapsed time in the case of Fig.9(b). The typical major semi-radius was 36.5 ± 0.5 mm and the minor one was less than 1 mm. Both the radii remained approximately constant throughout the measurement. The major radius was calculated by the method of least squares from the image. It was, on the other hand, difficult to directly determine the minor one from the images because of very thin ellipses. A principal component analysis (PCA) allowed the minor radius to be determined for the observed data.

Figure 10 show typical temporal behaviors of the rotation angle ψ_2 , the action J_2 and the rotation rate ω_2 from the top to the bottom for two cases of $d \simeq d_{\text{opt}}$ and of $d < d_{\text{opt}}$. In the case of $d \simeq d_{\text{opt}}$, the rotation angle linearly decreased in magnitude, resulting in the averaged rotation rate of $\langle \omega_2 \rangle = -8.63$ deg/h; in the case of $d < d_{\text{opt}}$, $\langle \omega_2 \rangle = -7.93$ deg/h. Comparing the measured results on temporary behaviors of the action and the rotation rate with the calculated ones as shown in

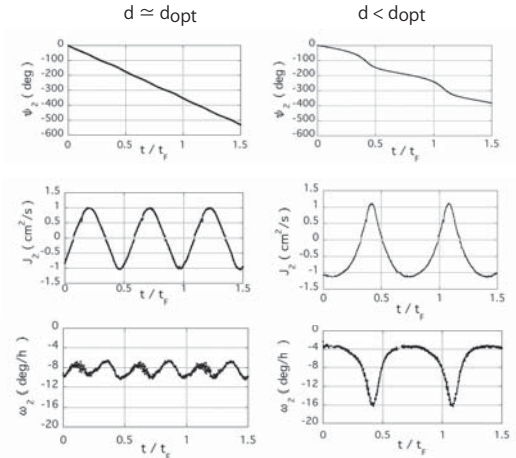


Fig. 10. Measured temporal behaviors of ψ_2 , J_2 per unit mass, and ω_2 from the top to the bottom. The figures in the left and right sides correspond to the case of $d \simeq d_{\text{opt}}$ and to that of $d < d_{\text{opt}}$, respectively.

Fig.3 and 4, we recognize strong resemblances to each others. We also observe the higher harmonics oscillation of the rotation rate at $d \simeq d_{\text{opt}}$. For $d < d_{\text{opt}}$, ω_2 oscillates out of phase with respect to J_2 .

The characteristics in the temporal behaviors can be explained by using the Adler's equation as described in the previous section. Figure 11, for a example, shows measured periods as a function of the distance, d . The solid curve was numerically obtained by solving eqs.(19) and (20) with the relevant parameters. The broken curve in the figure shows periods calculated by using the equation of $\pi/\Omega_F \sqrt{1-\beta^2}$ derived from the Adler's equation (25). In the region near d_{opt} the two curves were very similar. Apart from the optimal distance, the period increased as expected in the present analysis even when the distance became larger as well as smaller than d_{opt} . The experimental results were in an excellent agreement with the numerical calculated ones as shown in the figure.

In the circumstance we focus on the optimal performance of the Foucault pendulum. As seen in the previous section, a short-term measurement did not always lead to the optimal condition realizing the ideal Foucault rotation rate. Because of lack of precise knowledge as to the asymmetry on the system, the condition should not be *a priori* exactly determined from the analysis, but could be *a posteriori* obtained through a long-term measure-

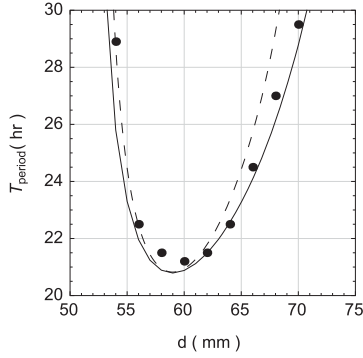


Fig. 11. Periods of the action J_2 as a function of the distance d . The filled circles represent measured periods for the action. The solid curve is numerically determined by solving eqs.(19) and (20) with parameters of $\lambda = 2 \text{ h}^{-1}$ and $\delta_0 = 0.4$. The broken one is analytically determined by using the period of $\pi/\Omega_F \sqrt{1 - \beta^2}$ with the same parameters.

ment.

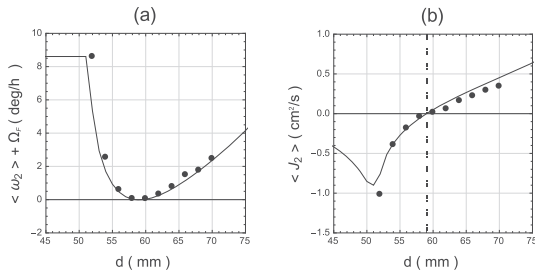


Fig. 12. Experimental results at Kyoto; (a): difference of the average rotation rate $\langle \omega_2 \rangle$ from the Foucault one, $-\Omega_F = -8.63 \text{ deg/h}$ at Kyoto, (b): the average action variable $\langle J_2 \rangle$ per unit mass; the broken line to the distance, d_{opt} , corresponding to $\langle J_2 \rangle = 0$. The filled circles represent measured data and the solid curves were numerically calculated for eqs.(19) and (20) with parameters of $\lambda = 2 \text{ h}^{-1}$ and $\delta_0 = 0.4$.

Figure 12 shows the average rotation rate and the average action over one rotation period at Kyoto. As seen from the figure, the experimental results showed an excellent agreement of the calculated ones with relevant parameters. It was, however, difficult to distinguish the "ideal Foucault rotation rate", $-\Omega_F$, from others near d_{opt} . It was, on the other hand, much easier to find out d_{opt} , at which $\langle J_2 \rangle = 0$ as shown in the Fig.12(b). Consequently the pendulum was able to succeed

in the optimal performance when the average action $\langle J_2 \rangle$ vanished as a result of nullifying the surplus rotation due to the elliptical motion with the magnetic force by the pair of the permanent magnets. This was completely different from the result with a brief observation as reported in the references.^{10, 13)}

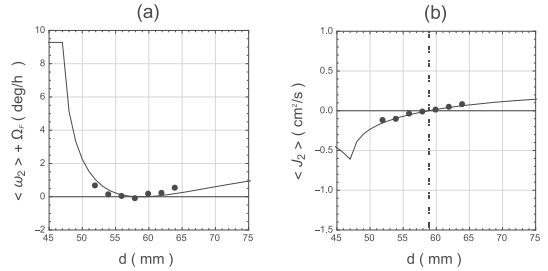


Fig. 13. Experimental results at Yamagata; (a): difference of the average rotation rate $\langle \omega_2 \rangle$ from the Foucault one, $-\Omega_F = -9.31 \text{ deg/h}$ at Yamagata, (b): the average action variable $\langle J_2 \rangle$ per unit mass; the broken line to the distance, d_{opt} , corresponding to $\langle J_2 \rangle = 0$. The filled circles represent measured data and the solid curves were numerically calculated for eqs.(19) and (20) with parameters of $\lambda = 2 \text{ h}^{-1}$ and $\delta_0 = 0.2$.

As expected in eqs.(19) and (20), the optimal condition must be independent of a latitude. For the purpose of examining such the expectation about optimal condition, the present portable device was transferred, set and operated at Yamagata. The first reason why Yamagata was selected was its location. The latitude difference is large enough to distinguish the Foucault rotation rate from that in Kyoto; Yamagata is at the latitude of $38^\circ 14' N$, and the corresponding to the Foucault rotation rate is -9.31 deg/h . The other reason, which was more important, was that we were available for a staff supporting and a facility usage essential to a long-term operation of the device. Figure 13 shows the average rotation rate and the average action over one rotation period measured in Yamagata. As seen from Fig.13(b), the optimal distance, which nullifies the surplus rotation, remained the same distance as that measured in Kyoto when the action $\langle J_2 \rangle = 0$. Consequently it is confirmed that once the optimal condition was experimentally found, the pendulum were able to be operated in the "ideal" Foucault pendulum performance with the same distance d_{opt} even at different

latitudes.

In the experiment it was observed sufficiently small amplitude of higher harmonic oscillation in the rotation rate at $d \simeq d_{\text{opt}}$. One possible mechanism causing such the small amplitude might be an asymmetric effect due to the difference between the moments of inertia around two axes of X and Y through the supporting point as shown in Fig.7. The system was symmetrical below the supporting point, resulting in equal moment in magnitude. Therefore the asymmetry might be caused by the supporting itself. The moment of inertia around the X-axis was $I_X = m_{\text{ke}}(5a_{\text{ke}}^2/12)$ contributed only from the upper triangular prism, where m_{ke} , a_{ke} and h_{ke} were the mass, the one side length and the length of the prism, respectively. On the other hand, the moment of inertia around the Y-axis was contributed not only from the triangular prism but also from the disk, so that $I_Y = m_{\text{ke}}(3a_{\text{ke}}^2/8 + h_{\text{ke}}^2/12) + m_{\text{disk}}/4 \cdot (R_1^2 + R_2^2 + H^2/4)$, where m_{disk} , R_1 , R_2 and H were the mass, the inner and outer radii, and the depth of the annular disk, respectively. The difference between the moments was $\Delta I = I_Y - I_X = m_{\text{ke}}(h_{\text{ke}}^2/12 - a_{\text{ke}}^2/24) + m_{\text{disk}}/4 \cdot (R_1^2 + R_2^2 + H^2/4)$. Total moment of inertia, I_{total} , was approximately equal to the moment of inertia of the bob around the X-axis or the Y-axis; $I_{\text{total}} \simeq m_{\text{bob}}(R_{\text{bob}}^2/4 + 19L_{\text{bob}}^2/12) + m_{\text{bob}}\ell_0^2$, where m_{bob} , R_{bob} , and L_{bob} were the mass, the radius and the length of the cylindrical bob, respectively. In the experiment, we had $m_{\text{ke}} = 11.9\text{g}$, $h_{\text{ke}} = 3.5\text{cm}$ and $a_{\text{ke}} = 1\text{cm}$ for the triangular prism, $m_{\text{disk}} = 69.4\text{g}$, $R_1 = 0.5\text{cm}$, $R_2 = 1.75\text{cm}$, $H = 1\text{cm}$ for the annular disk, and $m_{\text{bob}} = 2.4\text{kg}$, $R_{\text{bob}} = 3\text{cm}$ and $L_{\text{bob}} = 10\text{cm}$ for the bob. The ratio of the moment difference to the total moment of inertia was approximately $\Delta I/I_{\text{total}} \simeq 3.43 \cdot 10^{-6}$. Supposing that the difference was equal to the asymmetric coefficient, namely, $\delta (= \delta_0 \cdot \Omega_F / \omega_0) = \Delta I / I_{\text{total}}$, we obtained the expected coefficient of $\delta_0^{\text{the}} = 0.26$. On the other hand, the observed variation in ω_2 was typically $\Delta\omega^{\text{exp}} = 3 \text{ deg/h}$ for $d \simeq d_{\text{opt}}$ as seen from Fig.10. By using eqs.(19) and (24) with the observed amplitude, $\Delta\omega^{\text{exp}}$, we could obtain the equation of $\delta_0^{\text{exp}} = \sqrt{\lambda} \cdot \Delta\omega^{\text{exp}} / \Omega_F$, which yielded $\delta_0^{\text{exp}} \simeq 0.28$.

The asymmetric coefficient, δ_0 , best fitting with the experimental result of both the rotation rate and the action was a factor of 1.4 in Kyoto, and a factor of 0.71 in Yamagata to δ_0^{exp} . These results

indicated that the small amplitude in ω_2 observed at $d \simeq d_{\text{opt}}$ might resulted from the asymmetric effect due to the difference between the moments of inertia.

The present experiments exhibited the limit-cycle oscillation and sometimes brought about the locking phenomena. For the case of $[1 - (\omega_b/\Omega_F)^2] > 0$, the stable limit cycle oscillations were observed as seen from the Figs.12 and 13. The locking phenomena happened when the rotation rate satisfied the equality of $|\omega_b/\Omega_F| = 1$. The equality is rewritten as follows;

$$\frac{6\delta_0 J_1 \cdot (1 - f_{\text{mag}})}{8m\ell_0^2 \lambda} = \begin{cases} 1 & \text{for } d > d_{\text{opt}}, \\ -1 & \text{for } d < d_{\text{opt}}. \end{cases} \quad (28)$$

For the present movable range of the distance from 40 mm to 70 mm, the factor of $(1 - f_{\text{mag}})$ as a function of the distance monotonically increased from -3.834 to $+0.534$ for the relevant parameters. Consequently in the present experiment the locking phenomena happened in the region of $40 \text{ mm} < d < d_{\text{opt}}$ for $\delta_0 > 0.08$; in the region of $70 \text{ mm} > d > d_{\text{opt}}$ they might occur when the asymmetry satisfied the inequality of $\delta_0 > 0.58$.

At the end of this section, we mention the damping of the transversal component of motion. Earthquakes were sometimes experienced while operating the device because it was *Japan*. They, by chance, gifted us an experimental result of the damping of the transversal component for motion of the pendulum. Figure 14 shows temporal behaviors of ψ_2 , ω_2 and J_2 recorded when an earthquake suddenly disturbed the motion of the pendulum. The seismic intensity was less than 1 at the laboratory of Kyoto University and was too small for us to experience. We observed a break in the line of the rotation angle just when the earthquake occurred, as shown in Fig.14(a). The rotation angle abruptly advanced approximately 7.6 degrees during 10 minutes in the clockwise direction. At this time the rotation rate increased in the clockwise direction by 2.5 times or more in a spike shape as shown in Fig.14(b). At the same time the action rapidly increased in the direction to compensate the rapid increase in the rotation by the law of inertia. After a few hours, the pendulum recovered its previous motion without other residual effects.

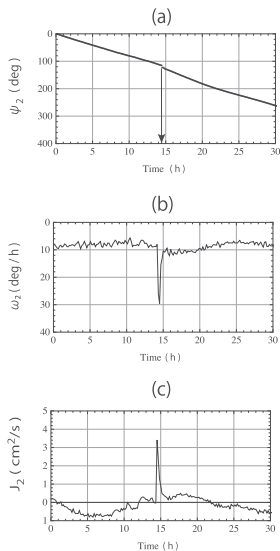


Fig. 14. Temporal behaviors of ψ_2 , ω_2 and J_2 observed for the pendulum when an earthquake of the intensity less than 1 took place in Kyoto; from the top to the bottom, (a), (b) and (c) correspond to the rotation angle, the rotation rate and the action, respectively. The earthquake occurred at the time indicated by the arrow in Fig.(a).

The typical damping time of the action was estimated to be half an hour from the observed result as shown in Fig.14(c). Therefore, we have adopted $\lambda \simeq 2 \text{ h}^{-1}$ in general as the damping coefficient of the action in the present analysis.

4. Conclusion

We analyzed the motion in a portable Foucault pendulum by both experimental and numerical approaches. A theoretical model was formulated by considering the effects of the elliptical motion, the magnetic field and the asymmetry, and also the dissipation due to the eddy current induced by the permanent magnet into the disk. The experimental pendulum had both driving and damping, and its motion was observed in detail with a webcam. After parameter identification, numerical calculations showed an excellent agreement with the experimental results. The present portable device made the ideal Foucault performance when the average action vanished. It was experimentally proved that the pendulum was able to realize the Foucault performance corresponding to the latitude when the same optimal condition was set for the pendulum even at a different latitude. Shortcoming in difference between the moments of in-

ertia, which brought about the small asymmetry, would be overcome by development of a more symmetric support.

Some limitations, however, are worth noting to develop new table-size pendulums, which can be easily utilized for educational purposes and investigations of various nonlinear phenomena. Further reduction to the table-size device might require alternative method and device for successful operation.

Furthermore, limit cycle motion and locking phenomenon were observed, depending on the distance between the control magnets. The criterion to the locking phenomena could be estimated by using the Adler's equation. Chaotic and locking phenomena themselves, however, should require follow-up investigations in future works.

Acknowledgments

We want to thank Y. Yamashita, M. Tetsuo and K. Arimura for valuable discussions about the locking phenomena in particular. We deeply acknowledge Professor M. Kitaura and his colleagues for continuous encouragement and support on operations of the device at Yamagata University. We also acknowledge Professors N. Fujiwara and T. Kinoshita for their encouragements. Finally we thank the referees for careful examination of our manuscript.

Appendix: Asymmetric Potential

In this appendix we give the asymmetric potential in the terms of canonical action-angle variables of ψ_1, ψ_2, J_1 and J_2 . The gravitational potential energy V for the mass of pendulum, m , is given by

$$V = mgz = mg\ell_0(1 - \cos \theta), \quad (\text{A.1})$$

$\cos \theta = \sqrt{1 - \sin^2 \theta} = \sqrt{1 - (x^2 + y^2)/\ell_0^2}$. Here we introduce the asymmetry in the coordinates of x, y into the potential as follows;

$$x^2 + y^2 \longrightarrow (1 + \delta)^2 \cdot x^2 + (1 - \delta)^2 \cdot y^2. \quad (\text{A.2})$$

where, δ is the asymmetric coefficient of order $O(\delta) \sim O((x/\ell_0)^2), O((y/\ell_0)^2) \ll 1$. Expanding the above equation until the fourth power of x/ℓ_0 and

y/ℓ_0 , we obtain the following equation,

$$\begin{aligned} V &= mgz \\ &= mg\ell_0 \left[\frac{1}{2} \frac{x^2 + y^2}{\ell_0^2} + \frac{1}{8} \left(\frac{x^2 + y^2}{\ell_0^2} \right)^2 + \delta \frac{x^2 - y^2}{\ell_0^2} \right] \\ &\simeq mg\ell_0 \left[\frac{1}{2} \theta^2 - \frac{1}{24} \theta^4 + \delta \cos 2\phi \theta^2 \right]. \quad (\text{A}\cdot 3) \end{aligned}$$

where, the first term in the braces of the r.h.s. represents the harmonic oscillation, the second one the nonlinear oscillation, and the last one the asymmetric oscillation. By replacing δ by $\delta_0 = \delta/(\Omega_F/\omega_0)$, the asymmetric term,

$$V_{\text{Asym}}(\theta, \phi) = \delta_0 m \omega_0 \Omega_F \ell_0^2 \cos 2\phi \theta^2, \quad (\text{A}\cdot 4)$$

is rewritten by using the action-angle variables of ψ_1, ψ_2, J_1 , and J_2 as follows;

$$\begin{aligned} V_{\text{Asym}}(\psi_1, \psi_2, J_1, J_2) &= \delta_0 \Omega_F J_1 \\ &\times \cos 2\psi_2 \left(\cos 2\psi_1 - \left[1 - \frac{J_2^2}{J_1^2} \right]^{1/2} \right) \\ &+ \sigma \delta_0 \Omega_F J_1 \sin 2\psi_2 \left| \frac{J_2}{J_1} \right| \sin 2\psi_1, \quad (\text{A}\cdot 5) \end{aligned}$$

where $\sigma = \pm 1$ for $J_2/|J_2|$. Time-averaging the asymmetric potential over the oscillation period lead to the equation given by

$$\begin{aligned} \langle V_{\text{Asym}} \rangle &= \frac{\omega_0}{2\pi} \int_0^{2\pi} V_{\text{Asym}} dt \\ &= -\delta_0 \Omega_F J_1 \cos 2\psi_2 \left(1 - \frac{J_2^2}{J_1^2} \right)^{1/2}. \quad (\text{A}\cdot 6) \end{aligned}$$

bits of the forced spherical pendulum” *Physica D: Non-linear Phenomena* 165, 1-11 (2002).

- 4) R.A. Nelson and M. G. Olsson: “The pendulum - Rich physics from a simple system” . *American Journal of Physics* 54 (2), 112-121 (1986).
- 5) A.S.dePaula, M. Savi and F.H.I.P. Pinto: “Chaos and transient chaos in an experimental nonlinear pendulum”, *Journal of Sound and Vibration* 294 585–595 (2006).
- 6) Heike Kamerlingh Onnes, Groningen dissertation, “Nieuwe Bewijzen voor de aswenteling der aarde.” (1879)
- 7) Schulz-Dubois, E.O., ‘Foucault Pendulum Experiment by Kammerlingh Onnes and Degenerate Perturbation Theory’ , *American Journal of Physics* 38(2), 173-188 (1970).
- 8) H. Kruglak and R. Pittet, ‘Portable, Continuously Operating Foucault Pendulum’ , *American Journal of Physics* 48(5), 419-420 (1980).
- 9) H.R. Crane, ‘Short Foucault Pendulum: A Way to Eliminate Precession Due to Ellipticity’ , *American Journal of Physics* 49(11), 1004-1006 (1981).
- 10) H.R. Crane, ‘Foucault pendulum ” wall clock”’ , *American Journal of Physics* 63(1), 33-39 (1995).
- 11) G. Mastner, V. Vokurka, M. Maschek, E. Vogt, and H. P. Kaufman, “Foucault pendulum with eddy-current damping of the elliptical motion”, *Rev. Sci. Instrum.* 55 (10), 1533 (1984).
- 12) H.G. Salva, R.E. Benavides, J.C. Perez, and D.J. Cuscueta, “A Foucault pendulum design”, *Rev. Sci. Instrum.* 81, 115102 (2010).
- 13) K.T. Hecht, ‘The Crane Foucault Pendulum: An Exercise in Action-angle Variable Perturbation Theory’ , *American Journal of Physics* 51(2), 110-114 (1983).
- 14) H. Goldstein, C. Poole and J. Safko, *Classical Mechanics*, (Pearson Education Inc. 2002); J.V. José and E.J. Saletan, *Classical Dynamics - A contemporary approach* (Cambridge University Press. 1998)
- 15) R. Adler, ‘A Study of Locking Phenomena in Oscillators’ , *PROCEEDINGS OF THE IEEE*, 1973, VOL. 61, NO. 10, 1380.
- 16) <http://opencv.org>

-
- 1) <http://www.atlasobscura.com/places/pantheon-paris>.
 - 2) <https://www.britannica.com/science/Foucault-pendulum>, <http://www.physics.uoguelph.ca/foucault/F6.html>, and <http://www.kahaku.go.jp/exhibitions>.
 - 3) T.J. Bridges and K.V. Georgiou: “Computing global or-

自立型フーコー振子の最適運転

道下 敏則*, 高橋 輝雄

京都大学大学院 人間・環境学研究科 相関環境学専攻

〒606-8501 京都市左京区吉田二本松町

この論文で、可搬型で自立型の小型フーコーの振り子が理想的な振る舞いを実現する新しい方法が記述される。振り子の回転角の位相とその角作用に対する二次元の摂動ハミルトン方程式の解析結果から、フーコーの振り子はフーコーの回転時間以上にわたり平均化された角作用がゼロとなる場合に理想的な振る舞いを呈することが新たに予測された。これは、角作用の詳細な観測実験によって、十分に実証された。フーコーの回転速度自身は緯度に依存するが、開発された装置で異なる緯度における観測結果から、理想的フーコーの回転を実現する制御パラメーターの最適化条件自身は緯度依存性がない事が確認された。さらに、制御用パラメーターに依存して、振り子の回転のリミットサイクル運動や位相のロッキング現象も観測された。これらの現象の発生条件は、アドラー方程式を用いて検討された。